INL/EXT-19-56012

Light Water Reactor Sustainability Program

Progress on Grizzly Development for Reactor Pressure Vessels and Reinforced Concrete Structures

Benjamin W. Spencer
William M. Hoffman
Daniel Schwen
Sudipta Biswas

September 2019

DOE Office of Nuclear Energy

INL/EXT-19-56012

Light Water Reactor Sustainability Program

Progress on Grizzly Development for Reactor Pressure Vessels and Reinforced Concrete Structures

Benjamin W. Spencer
William M. Hoffman
Daniel Schwen
Sudipta Biswas

Idaho National Laboratory

September 2019

Idaho National Laboratory
Idaho Falls, Idaho 83415

http://www.inl.gov/lwrs

Prepared for the
U.S. Department of Energy
Office of Nuclear Energy
Under DOE Idaho Operations Office
Contract DE-AC07-05ID14517

ABSTRACT

The Grizzly code has been under development for the U.S. Department of Energy's Light Water Reactor Sustainability program to provide predictive tools for the evolution of material degradation in critical light water reactor structural components due to long-term exposure to the environmental conditions of normal reactor operation, and for the effects of this degradation on the safety of these components. This development has primarily targeted reactor pressure vessels and reinforced concrete structures. Work performed during Fiscal Year 2019 added important features for both of these types of structures.

For probabilistic fracture mechanics analysis of reactor pressure vessels, capabilities were added to account for the effects of warm prestressing and residual stresses, as well as to model crack initiation, growth, and arrest. For modeling microstructure evolution in reactor pressure vessels, a cluster dynamics model for evolution of Mn-Ni-Si phases has been implemented. For modeling degraded reinforced concrete structures, capabilities to consider the combined effects of damage and creep in the concrete constitutive model and model nonlinear behavior of reinforcing bars has been added.

These newly-developed features fill important gaps in Grizzly's feature set for engineering-scale analysis of degraded reactor pressure vessels and reinforced concrete structures. Grizzly development in both of these areas has reached a point where it is ready for extensive testing on relevant engineering problems.

CONTENTS

FIGURES

ACRONYMS

ASR	alkali-silica reaction
ASME	American Society of Mechanical Engineers
CPF	conditional probability of failure
CPI	conditional probability of fracture initiation
LEFM	linear elastic fracture mechanics
LWR	light water reactor
LWRS	Light Water Reactor Sustainability
MNSP	Manganese-Nickel-Silicon precipitate
ODE	ordinary differential equation
PFM	probabilistic fracture mechanics
RIVE	radiation-induced volumetric expansion
RPV	reactor pressure vessel
SIFIC	stress intensity factor influence coefficient

1 Introduction

Long-term exposure to the environmental conditions that exist in operating light water reactor nuclear power plants can cause degradation of the materials from which critical components of these plants are constructed. When considering long term operation of existing LWRs, it is important to understand the extent of this degradation and its effect on the safety of these structures, to ensure that these plants can continue to operate safely for an extended time. The Grizzly code is being developed to address these issues, and has models to predict the evolution of degradation mechanisms and their effects on structural integrity.

Grizzly has capabilities that have been under development to address two major types of LWR structures: reactor pressure vessels and reinforced concrete structures. The tools for engineering-scale analyses of these structures are maturing, but some important components have still been missing that have limited Grizzly's applicability to practical problems of interest. This report documents work funded by the U.S. Department of Energy's Light Water Reactor Sustainability (LWRS) program during Fiscal Year 2019 to address these needs. This work is in three major areas:

- **Engineering-scale Reactor Pressure Vessel Analysis**: This area has been a major focus of recent development. Grizzly already had a reasonably complete capability for performing probabilistic fracture mechanics (PFM) analysis of embrittled reactor pressure vessels (RPVs), but it was missing some important features. This year RPV PFM capabilities were developed to account for three important phenomena: warm prestressing, residual stress, and fracture initiation, growth, and arrests models. This work brings Grizzly to the point where it has the majority of the features needed for this type of analysis.

- **Reactor Pressure Vessel Steel Microstructure Evolution**: An important research area for RPV integrity is understanding the effects of exposure to irradiation and elevated temperature on RPV steel over times beyond available experimental data. A major component of Grizzly development work has focused on developing predictive models for microstructure and engineering property evolution to help address the knowledge gaps in experimental data. The ability to predict the evolution of evolution of Mn-Ni-Si phases is important for understanding for RPV steel will behave under long-term exposure to the reactor environment. A cluster dynamics model for evolution of these phases has been developed in Grizzly, and complements previously-developed cluster dynamics models in Grizzly for evolution of Cu-rich phases.

- **Engineering-Scale Reinforced Concrete Mechanics**: Grizzly has a unique multiphysics modeling capability for concrete structures that predicts coupled phenomena of moisture and heat transport, expansive swelling, and mechanical deformation. This permits modeling the progression of degradation mechanisms such as alkali-silica reaction (ASR) and radiation-induced volumetric expansion (RIVE) in engineering-scale models of concrete structures. An important component of this tool that has been lacking is the ability to represent the nonlinear mechanical response of the structure, including damage, fracture, and yielding of reinforcing bars. Development documented here has added the ability to model the combined effects of creep and damage in the concrete constitutive model and to model nonlinear behavior in the 1D truss elements that are used to represent the effects of reinforcement in 2D or 3D finite element models of reinforced concrete structures.

The following major sections of this report describe in sequence the development in the areas described above.

2 Engineering-Scale Reactor Pressure Vessel Analysis

Development of a robust capability for engineering-scale probabilistic fracture mechanics (PFM) has been an important part of Grizzly development. Extensive work has been performed in the LWRS program to characterize and model material degradation, and it is important to have a tool to make the results of this research available to end users for engineering analysis. The algorithms used by Grizzly for PFM analysis of RPVs are based largely on the FAVOR code [1], which is widely accepted to be a state of the art code in this area, and embodies the results of multiple decades of research. Grizzly brings several important benefits over existing PFM codes, which are outlined in a recent paper[2] that demonstrates Grizzly's unique capabilities for this type of analysis:

- **Modular Architecture** Grizzly is based on the MOOSE framework [3], which provides a foundation for multidimensional, multiphysics analysis, and has a modular object-oriented architecture. This modular design philosophy is employed in Grizzly's PFM capability.
- **Multidimensional Capability** A number of important phenomena in RPVs, such as coolant plume effects [4] can only be represented by 2D or 3D models. Grizzly can model RPVs in 1D, 2D, or 3D, as appropriate for the phenomena to be considered.
- **General Flaw Geometry** Current codes are limited to evaluating axis-aligned flaws. The discovery of quasi-laminar flaws in Belgian reactors [5] demonstrated the need for a more general capability. Grizzly has general fracture mechanics capabilities that can be applied to arbitrary flaw geometries.
- **High Performance Computing** Grizzly is designed to take advantage of parallel computers (although it can be run on a single processor), which greatly reduces the computation time required for higher dimensionality simulations of RPV global response and for the Monte Carlo simulations used in PFM analysis.

The flexibility of Grizzly's modular architecture was recently demonstrated when it was adapted to permit reading of a 3D neutron fluence map provided the VERAShift code developed by the Consortium for Advanced Simulation of Light Water Reactors (CASL) [6]. This development was done by creating a new specialization of an existing class to obtain fluences from a different source.

Prior to the new work documented here, Grizzly already had a basic capability to perform PFM calculations, including those based on 2D or 3D models of the global RPV thermo-mechanical response to a transient loading. However, it was missing capabilities to account for the effects of warm prestressing, residual stresses, and fracture arrest, all of which can have an important effect on the outcome of a PFM analysis. Details of these phenomena and the model development to address them are described below.

2.1 Warm Prestressing

Warm prestressing is a phenomenon that occurs when the fracture toughness of a material increases due to being previously stressed at a high temperature. There are three mechanisms by which this is understood to occur. First, preloading at an elevated temperature work hardens the material ahead of the crack tip. Secondly, the same preloading at elevated temperatures can cause blunting of the crack tip, which reduces the geometric stress concentration. Finally, rapid cooling near the crack tip produces compressive residual stresses ahead of the crack tip, increasing the load required to open the crack.

The primary objective of a PFM analysis is to compute the conditional probability of fracture initiation (CPI) for given occurrence of an event that induces a transient loading on an RPV. This based on the aggregate CPI of each individual flaw. The fracture toughness is temperature-dependent, and the statistical models used

indicate nonzero CPI when the applied stress intensity factor K_I is greater than the minimum value of K_I for nonzero probability of fracture initiation at the current temperature, $K_{Ic\min}$.

The same models for accounting for warm prestressing used in FAVOR have been implemented in Grizzly. There are multiple models that account for warm prestressing, and they all require the following three conditions to be met for a nonzero probability of fracture initiation during a given time step of a transient:

1. K_I must be greater than $K_{Ic\min}$.
2. The applied K_I field is currently increasing with time.
3. The value of K_I for a given flaw at the current time must exceed a previously established maximum value of $K_{I(max)}$, times a factor α:

$$K_I(\tau) \geq \alpha K_{I(max)}(\tau) \tag{1}$$

If these conditions are met, CPI is computed using the aforementioned statistical model. The variants of the warm prestressing model are defined as follows:

1. If no warm prestressing model is used (i.e. warm prestressing is not accounted for), only condition 1 above must be met for nonzero CPI. This is the most conservative of the available options.
2. The "baseline" model requires that all 3 conditions are met, and assumes $\alpha = 1$.
3. The "conservative" model assumes $\alpha = 0$. This effectively means that only conditions 1 & 2 are met, because condition 3 is always met in this case.
4. In the "best estimate" model, α is a randomized parameter, and is sampled from a log-logistic distribution) see [7]. α can be greater than 1 in this case, which means that in some cases, K_I must significantly exceed $K_{I(max)}$ for a nonzero CPI.

All of these options have been implemented in Grizzly. To demonstrate the effects of the choice of warm prestressing model, all of the models have been tested on a single flaw, and the time history of CPI is examined. The flaw geometry was chosen from one of the benchmark problems used for assessing Grizzly's ability to correctly compute K_I during a transient. The flaw is a surface breaking flaw with a depth of 30% of the wall thickness and an infinite aspect ratio. This case was chosen because of its particularly high K_I as well as the fact that in this transient, the K_I history contains many local maxima and minima - ideal for demonstrating the various warm prestressing models. The pressure and temperature boundary conditions applied in this problem are shown in Figure 1.

The resulting time histories of K_I and the instantaneous and maximum CPI are shown in Figure 2 (where the maximum CPI is the maximum value of CPI up to the current point in time). As would be expected, the most conservative case is when there is no warm prestressing model, which results in the highest values of both instantaneous and maximum CPI. The "conservative" model is the next most conservative case, and it can be seen that it gives the same values of CPI as with no warm prestressing when K_I is increasing, but gives 0 otherwise. The "baseline" model only computes nonzero CPI during the late pressure spike, when K_I exceeded an earlier maximum value. Finally, the least conservative result is the "best estimate" model (with a prescribed $\alpha = 1.15$). This model computes a value of zero for CPI for this flaw because K_I does not sufficiently exceed the prior maximum value, which occurred when the temperature was high enough that CPI was zero. α is randomly sampled, and doesn't always exceed 1, so this model is not always less conservative than the "baseline" model, but this illustrates how this model would behave with a high value for α.

Figure 1: Temperature and pressure boundary conditions applied to the RPV model

Figure 2: Demonstration of all available warm prestressing models on the same single flaw. (top) K_I history for surface breaking flaw. (middle) Instantaneous CPI history with the three different models of warm prestressing, as well as with no warm prestressing model for comparison. (bottom) Maximum CPI history for this same set of models. In the best estimate model, a prescribed value of $\alpha = 1.15$ is used.

2.2 Weld Residual Stress

To construct an RPV, it is necessary to weld together several large plates or cylindrical forgings. The weld zones resulting from this process are typically several inches wide and pass through the thickness of the vessel wall. Weld regions are particularly susceptible to fracture and often contain residual stresses that were not completely relaxed by the post-weld heat treatment [8, 9]. A significant effort was taken to characterize these residual stresses, and the FAVOR code has had the ability to account for their effects on fracture for some time [1]. This important capability was previously missing from the Grizzly code, and the efforts to implement this in Grizzly (closely following the FAVOR approach) are documented here.

To consider residual stress effects, the through wall residual stress profile must first be defined. The welding process can be directly simulated using finite element codes to compute this, although this would be difficult to do for every RPV simulation. Grizzly currently does not simulate welding processes, though some preliminary investigation into adding these capabilities is currently underway. Because Grizzly can represent the global RPV response with a full 3D model, it would be possible to directly include the development of weld residual stresses in the RPV model used by Grizzly. This is an interesting potential research area, but the FAVOR approach, described here, is followed because it is more usable in practical application.

FAVOR considers weld residual stresses in probabilistic and deterministic flaw analysis models without actually simulating the welding process. The methodology used to obtain accurate residual stress data is documented well in [1]. This approach combines both physical and analytical modeling and determines the residual stress profile through the thickness of the vessel. A through-wall residual stress profile for a single wall thickness (8.936 in) was developed through a combination of experimental measurements of welded sections and simulation of the welding process. The resulting stress profile is used to describe both axial and hoop stress, which is scaled for any reasonable wall thickness of interest. The data collected from this study describing the through wall stress profile is shown in Figure 3.

This through-wall residual stress distribution is added to the stresses induced by the internal pressure and temperature gradients resulting from the transient loading scenarios being modeled. This residual stress is only applied to weld regions, although in the future more analysis can be performed to better characterize the effects of welding on the edges of plates and forgings.

The same residual stress profile is used for axial and circumferential flaw orientations, although the manner in which that is applied differs for surface breaking flaws and embedded flaws. There is currently no implementation for off-axis flaws although that would be relatively straightforward to implement because it would follow the same methodology.

2.2.1 Surface Breaking Flaws

Stress intensity factors are computed using the reduced order modeling approach of [10], which utilizes the principle of superposition under the assumption that linear elastic fracture mechanics (LEFM) is applicable. This approach assumes that the mode-I stress intensity factor, K_I, can be represented as a linear combination of the effects of multiple components of a polynomial representation of the through-wall variation of the stresses:

$$K_I = \sum_i^n w_i K_i \sqrt{\pi a} \tag{2}$$

This requires function weights w_i and stress intensity factor influence coefficients (SIFICs) K_i along with the length of the flaw a. The function weights are determined by fitting a polynomial to the through wall stress in the RPV. FAVOR uses a 3rd order polynomial, although recently developed SIFICs [11, 12] are based on the use of a 4th order polynomial to obtain a more accurate representation. The ASME Boiler & Pressure Vessel Code [13] provides closed-form expressions and tabular data for SIFICs for a variety of circumferential and axial elliptical and semi-elliptical flaws in thick-walled cylinders and plates in Section XI, Article A-3000.

Figure 3: Through wall weld residual stress data used by FAVOR [1]

These values stem from a library of pre-calculated stress intensity factor solutions capturing the effect of flaw and RPV geometry as it relates to different orders of stress polynomial approximation. This method was previously implemented in the Grizzly code and was benchmarked against both FAVOR models and detailed finite element models.

To consider residual stress effects with the previously described method, the residual stress profile is superimposed on the existing through wall stresses (induced by thermal or mechanical loads) by way of the function weights. The data in Figure 3 can be described using a 4th order polynomial, the coefficients of which are then added to the function weights in Equation 2 as shown in Equation 3 where w_{RS_i} is coefficient i of the polynomial used to describe the residual stress profile.

$$K_I = \sum_i^n (w_i + w_{RS_i}) K_i \sqrt{\pi a} \tag{3}$$

2.2.2 Embedded Flaws

The reduced order modeling procedure used for evaluating embedded flaws is different from that which is used for surface breaking flaws. The methodology implemented in both FAVOR and Grizzly for calculating Mode I stress-intensity factors of embedded (subsurface) flaws is based on older versions of Section XI, Article A-3000 of the ASME Boiler & Pressure Vessel Code:

$$K_I = (M_m \sigma_m + M_b \sigma_b) \sqrt{\pi a / Q} \tag{4}$$

where $2a$ is the minor axis of the elliptical subsurface flaw, Q is the flaw shape parameter, M_m and M_b are the free-surface correction factors for membrane stresses and bending stresses respectively, and σ_m and σ_b

are the membrane and bending stresses.

This method was previously implemented in Grizzly and benchmarked against FAVOR. It should be noted that this is known to contain significant conservatisms, and there are plans to replace this with the approach in the current version of the ASME code, which has a form more similar to that used for surface-breaking flaws. The components of Equation 4 affected by residual stresses are the membrane and bending stresses, which are defined as follows:

$$\begin{aligned} \sigma_m &= \frac{(\sigma(x_2) - \sigma(x_1))}{2a}(t/2 - x_1) + \sigma(x_1) \\ \sigma_b &= \frac{\sigma(x_1) - \sigma(x_2)}{a(t/2)} \end{aligned} \tag{5}$$

where $\sigma(x_1)$ and $\sigma(x_2)$ are the stress values in the wall corresponding to the nearest and deepest points on the crack from the inner surface of the RPV, and a is the crack length and t is the total wall thickness. To account for residual stresses, they are are added to the mechanically-induced stresses here. In Grizzly, these stresses are evaluated from an expansion of the polynomial used for surface-breaking flaws. Using the same polynomial describing the residual stress for surface breaking flaws, the stresses at each of the two points can be obtained, then added to the existing wall stress at those points:

$$\begin{aligned} \sigma(x_1) &= \sigma(x_1) - \sigma_{RS}(x_1) \\ \sigma(x_2) &= \sigma(x_2) - \sigma_{RS}(x_2) \end{aligned} \tag{6}$$

2.2.3 Benchmarking Residual Stress Effects on Axis Aligned Flaws

After implementing the weld residual stress effects in Grizzly, a number of cases were set up and analyzed to compare with FAVOR. These include axial and circumferential, surface breaking and embedded flaws, with and without a layer of .25 inch thick cladding. Flaw orientations align with the axes of the RPV, so flaws defined as circumferential are normal to the axial stress. For embedded flaws, a constant crack length of .24 inches was considered at depths of .96, 4.2 and 6.84 inches, and each depth was analyzed with aspect ratios of 2, 6, and 15. For surface breaking flaws, crack depths were .43, .86 and 2.58 inches, each with aspect ratios of 2, 6, 10 and infinite. A flaẃs aspect ratio is defined as L/a, so a perfectly circular flaw will have an aspect ratio of 2. See Figure 4 for definitions related to flaw geometry.

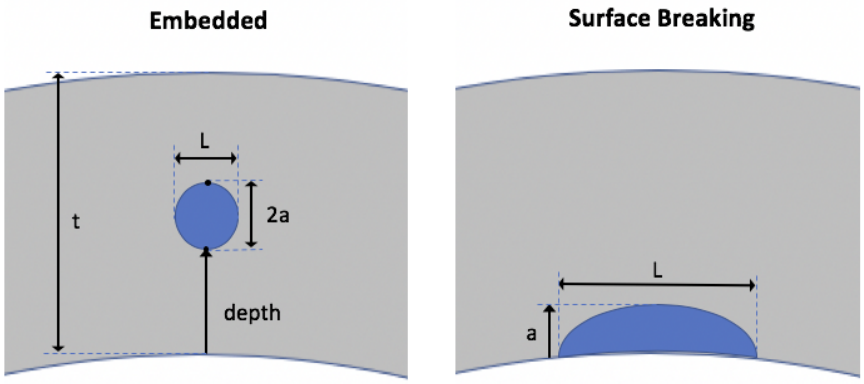

Figure 4: Embedded and surface breaking flaw definitions in Grizzly

These flaws were first evaluated with only the residual stresses, and no applied transient loading, The results of this study are shown in Table 1. The resulting stress intensity factors due to residual stresses show good agreement with the FAVOR results. Most of the surface breaking flaws have less than 10% difference between the two codes, the embedded flaws show a larger difference in some cases. The reason for these differences is apparent in Figure 5. The polynomial used to describe the residual stresses in the vessel is a 4th order polynomial, which is an does not perfectly fit the through-wall variation of the residual stress. The technique for applying the residual stresses in FAVOR differs from Grizzly's. For surface-breaking flaws, FAVOR uses a polynomial fit of the through-wall stress variation that is fit up to the flaw tip, rather than through the whole vessel wall. For embedded flaws, FAVOR directly looks up the stresses at the flaw tips, rather than using a polynomial. It is thus less sensitive to an imperfect representation of the stress variation by a polynomial.

It can be seen from Figure 5 that the polynomial tends to match the data more closely near the inner half of the vessel, which explains why the surface breaking flaws in Grizzly match more closely with FAVOR in that region. The embedded flaws used in this particular benchmarking study are deeper than the surface breaking flaws and thus to align with the areas of the polynomial that do not match the data as well, and tend to have higher errors.

Figure 5: Residual stress data including polynomial fits used to describe stress profile

Also shown in Figure 5 is a fitted 8th order polynomial, which is a better approximation than the 4th order polynomial. This cannot be used for surface breaking flaws because the SIFICs for those flaws used in Equation 2 do not support higher than 4th order polynomials. However, for embedded flaws, it is straightforward to sample the stresses from a higher order polynomial, and when that was done, the agreement between FAVOR and Grizzly was much better, as shown in Table 2.

Although the Grizzly results sometimes differ by a non-trivial amount from the FAVOR benchmark

Table 1: Comparison of K_I computations between Grizzly and FAVOR using a 4th order polynomial to describe the through wall residual stress

Surface Breaking With Clad

Flaw Orientation	Flaw	Grizzly	FAVOR	Difference	Diff %
Axial	d1_ar2	4.91	4.42	0.49	11.09
	d1_ar6	6.79	6.32	0.47	7.44
	d1_ar10	7.09	6.68	0.41	6.14
	d1_ar99	8.33	7.77	0.56	7.21
	d2_ar2	5.30	5.28	0.02	0.38
	d2_ar6	7.65	7.77	0.12	1.54
	d2_ar10	8.04	8.31	0.27	3.25
	d2_ar99	9.94	9.84	0.1	1.02
	d3_ar2	0.62	0.38	0.24	63.16
	d3_ar6	2.90	3.26	0.36	11.04
	d3_ar10	3.59	4.49	0.9	20.04
	d3_ar99	7.27	7.49	0.22	2.94
Circumferential	d1_ar2	4.91	4.42	0.49	11.09
	d1_ar6	6.79	6.32	0.47	7.44
	d1_ar10	7.09	6.68	0.41	6.14
	d1_ar99	8.69	8.07	0.62	7.68
	d2_ar2	5.30	5.28	0.02	0.38
	d2_ar6	7.65	7.77	0.12	1.54
	d2_ar10	8.04	8.31	0.27	3.25
	d2_ar99	10.07	9.95	0.12	1.21
	d3_ar2	0.62	0.38	0.24	63.16
	d3_ar6	2.90	3.27	0.37	11.31
	d3_ar10	3.59	4.51	0.92	20.40
	d3_ar99	4.98	6.26	1.28	20.45

Surface Breaking Without Clad

Flaw Orientation	Flaw	Grizzly	FAVOR	Difference	Diff %
Axial	d1_ar2	4.7	4.43	0.27	6.09
	d1_ar6	6.73	6.34	0.39	6.15
	d1_ar10	7.07	6.7	0.37	5.52
	d1_ar99	8.38	7.8	0.58	7.44
	d2_ar2	5.09	5.28	0.19	3.60
	d2_ar6	7.54	7.79	0.25	3.21
	d2_ar10	7.97	8.33	0.36	4.32
	d2_ar99	9.83	9.86	0.03	0.30
	d3_ar2	0.88	0.34	0.54	158.82
	d3_ar6	3.27	3.23	0.04	1.24
	d3_ar10	4.02	4.45	0.43	9.66
	d3_ar99	7.73	7.46	0.27	3.62
Circumferential	d1_ar2	4.7	4.43	0.27	6.09
	d1_ar6	6.73	6.34	0.39	6.15
	d1_ar10	7.07	6.7	0.37	5.52
	d1_ar99	8.71	8.1	0.61	7.53
	d2_ar2	5.09	5.28	0.19	3.60
	d2_ar6	7.54	7.79	0.25	3.21
	d2_ar10	7.97	8.33	0.36	4.32
	d2_ar99	9.94	9.97	0.03	0.30
	d3_ar2	0.88	0.34	0.54	158.82
	d3_ar6	3.27	3.23	0.04	1.24
	d3_ar10	4.02	4.47	0.45	10.07
	d3_ar99	5.46	6.23	0.77	12.36

Embedded With Clad 4th Order

Flaw Orientation	Flaw	Grizzly 4th	FAVOR	Difference	Diff %
Axial	d1_ar2	1.53	2.05	0.52	25.37
	d1_ar6	1.79	2.39	0.6	25.10
	d1_ar15	1.84	2.46	0.62	25.20
	d2_ar2	-1.7	-1.68	0.02	1.19
	d2_ar6	-1.98	-1.96	0.02	1.02
	d2_ar15	-2.04	-2.02	0.02	0.99
	d3_ar2	0.4	0.27	0.13	48.15
	d3_ar6	0.46	0.31	0.15	48.39
	d3_ar15	0.48	0.32	0.16	50.00
Circumferential	d1_ar2	1.53	2.05	0.52	25.37
	d1_ar6	1.79	2.39	0.6	25.10
	d1_ar15	1.84	2.46	0.62	25.20
	d2_ar2	-1.7	-1.68	0.02	1.19
	d2_ar6	-1.98	-1.96	0.02	1.02
	d2_ar15	-2.04	-2.02	0.02	0.99
	d3_ar2	0.4	0.27	0.13	48.15
	d3_ar6	0.46	0.31	0.15	48.39
	d3_ar15	0.48	0.32	0.16	50.00

Embedded Without Clad 4th Order

Flaw Orientation	Flaw	Grizzly 4th	FAVOR	Difference	Diff %
Axial	d1_ar2	1.5	1.9	0.4	21.05
	d1_ar6	1.75	2.22	0.47	21.17
	d1_ar15	1.81	2.28	0.47	20.61
	d2_ar2	-1.72	-1.77	0.05	2.82
	d2_ar6	-2	-2.07	0.07	3.38
	d2_ar15	-2.07	-2.13	0.06	2.82
	d3_ar2	0.41	0.23	0.18	78.26
	d3_ar6	0.48	0.27	0.21	77.78
	d3_ar15	0.49	0.27	0.22	81.48
Circumferential	d1_ar2	1.5	1.9	0.4	21.05
	d1_ar6	1.75	2.22	0.47	21.17
	d1_ar15	1.81	2.28	0.47	20.61
	d2_ar2	-1.72	-1.77	0.05	2.82
	d2_ar6	-2	-2.07	0.07	3.38
	d2_ar15	-2.07	-2.13	0.06	2.82
	d3_ar2	0.41	0.23	0.18	78.26
	d3_ar6	0.48	0.27	0.21	77.78
	d3_ar15	0.49	0.27	0.22	81.48

solutions when only considering residual stresses, these differences are relatively minor in the context of a transient analysis, where the total stress is typically dominated by that induced by the transient loading. Every flaw evaluated in Tables 1 and 2 was analyzed under representative transient thermal and mechanical loading with and without residual stresses, and the K_I history was plotted to quantify the difference between Grizzly and FAVOR results. Figure 6 shows a history of K_I for one of the cases in which the difference between the two codes was the most significant when only residual stresses were considered. Figure 7 shows a similar result for a case where the differences are more typical of the flaw geometries considered in this benchmarking study. Most of the cases show very small differences between the two codes.

Table 2: Comparison of K_I computations between Grizzly and FAVOR using an 8th order polynomial to describe the through wall residual stress

Embedded With Clad 8th Order					
Flaw Orientation	Flaw	Grizzly 8th	FAVOR	Difference	Diff %
Axial	d1_ar2	1.89	2.05	0.16	7.80
	d1_ar6	2.21	2.39	0.18	7.53
	d1_ar15	2.27	2.46	0.19	7.72
	d2_ar2	-1.73	-1.68	0.05	2.98
	d2_ar6	-2.01	-1.96	0.05	2.55
	d2_ar15	-2.07	-2.02	0.05	2.48
	d3_ar2	0.29	0.27	0.02	7.41
	d3_ar6	0.34	0.31	0.03	9.68
	d3_ar15	0.35	0.32	0.03	9.37
Circumferential	d1_ar2	1.88	2.05	0.17	8.29
	d1_ar6	2.19	2.39	0.2	8.37
	d1_ar15	2.26	2.46	0.2	8.13
	d2_ar2	-1.73	-1.68	0.05	2.98
	d2_ar6	-2.01	-1.96	0.05	2.55
	d2_ar15	-2.07	-2.02	0.05	2.48
	d3_ar2	0.29	0.27	0.02	7.41
	d3_ar6	0.34	0.31	0.03	9.68
	d3_ar15	0.35	0.32	0.03	9.37

Embedded Without Clad 8th Order					
Flaw Orientation	Flaw	Grizzly 8th	FAVOR	Difference	Diff %
Axial	d1_ar2	1.92	1.9	0.02	1.05
	d1_ar6	2.24	2.22	0.02	0.90
	d1_ar15	2.3	2.28	0.02	0.88
	d2_ar2	-1.73	-1.77	0.04	2.26
	d2_ar6	-2.02	-2.07	0.05	2.42
	d2_ar15	-2.08	-2.13	0.05	2.35
	d3_ar2	0.3	0.23	0.07	30.43
	d3_ar6	0.35	0.27	0.08	29.63
	d3_ar15	0.36	0.27	0.09	33.33
Circumferential	d1_ar2	1.92	1.9	0.02	1.05
	d1_ar6	2.24	2.22	0.02	0.90
	d1_ar15	2.3	2.28	0.02	0.88
	d2_ar2	-1.73	-1.77	0.04	2.26
	d2_ar6	-2.02	-2.07	0.05	2.42
	d2_ar15	-2.08	-2.13	0.05	2.35
	d3_ar2	0.3	0.23	0.07	30.43
	d3_ar6	0.35	0.27	0.08	29.63
	d3_ar15	0.36	0.27	0.09	33.33

Figure 6: KI history plots showing Grizzly comparison with FAVOR with and without residual stress effects, for a flaw geometry that has one of the largest differences between the two codes

Because the differences due to the way residual stresses are handled are relatively minor, the 4th order polynomial is currently being used in Grizzly. This will be re-evaluated when the newer approach for handling embedded flaws is implemented. The effects of residual stresses were evaluated here in deterministic

Figure 7: KI history plots showing Grizzly comparison with FAVOR with and without residual stress effects, for a flaw geometry that results in a fairly typical difference between the two codes

analyses of individual flaws. Further testing of the residual stress capability is required on large-scale PFM calculations of entire RPVs to ensure that this capability is functioning correctly in that context.

2.3 Fracture Initiation, Growth, and Arrest Model

The primary objective in a PFM analysis of an RPV under transient conditions is to evaluate the aggregate conditional probability of failure of the vessel given the presence of a population of flaws. The process for computing this aggregate CPI for the vessel (CPI_{RPV}) can be expressed as:

$$\text{CPI}_{\text{RPV}} = 1 - \prod_{i=1}^{n_{\text{flaw}}} (1 - \text{CPI}_i) \tag{7}$$

where n_{flaw} is the total number of flaws in the RPV, i is the flaw index, and CPI_i is the maximum value of CPI for flaw i during a given transient. Using CPI as a measure of the probability of a vessel rupture during a transient is inherently conservative because it assumes that if a crack initiates at any flaw location in the vessel, it will propagate through the vessel and the vessel will be breached. In reality, there is a reasonable likelihood that fractures will arrest before entirely propagating through the vessel.

To account for the possibility of crack arrest, a second metric, known as the conditional probability of failure or CPF, can also be evaluated. If failure is defined as a crack propagating through the vessel, CPF is the probability that a crack will propagate entirely through the wall of the vessel without arresting. For this to occur, a crack must first initiate, and only a subset of the initiated cracks will propagate through the wall, so by definition, CPF≤CPI.

If $P(F|I)$ is the probability of failure given fracture initiation, CPF for flaw i can be expressed as:

$$\text{CPF}_i = P(F|I)_i \times \text{CPI}_i \tag{8}$$

Once CPF is computed for every flaw in the vessel, the aggregate CPF for the vessel can be computed in the same manner as for CPI:

$$\text{CPF}_{\text{RPV}} = 1 - \prod_{i=1}^{n_{\text{flaw}}} (1 - \text{CPF}_i) \tag{9}$$

2.3.1 Description of Algorithm

A probabilistic analysis of each flaw with a nonzero CPI is performed to determine the likelihood of that flaw arresting before propagating through the vessel wall using what is known as a fracture initiation, growth, and arrest (IGA) model. As for the other aspects of the PFM capability, the Grizzly implementation of the IGA model is based on that of the FAVOR code.

IGA model makes the following fundamental assumptions:

- Once a crack initiates, it will initially propagate to its sides until it becomes an "infinite" surface-breaking crack before propagating through the thickness of the vessel.
- A crack will arrest when the stress intensity factor K_I is lower than the arrest threshold, K_{Ia}.
- The vessel can also fail due to plastic collapse if the remaining intact ligament has an insufficient thickness to support the current applied pressure.

Implementing this model involves code modules for sampling randomized values of K_I and computing the fraction of samples for which flaws do not arrest. For each random sample, a flaw is incrementally advanced through the wall, and K_I is compared to K_{Ia} at each increment to see whether the flaw arrests. The details of the various aspects of this model are described below.

Monte Carlo Sampling Loop The computation of CPI is based on Monte Carlo sampling in which each random realization represents a set of sampled parameters describing the population of flaws in an RPV. For a flaw to have a nonzero change in CPF during a step, it must have a nonzero and increasing value for CPI. Thus, the probabilistic calculation of $P(F|I)$ and CPF is performed only on the subset of flaws that meet those conditions (which is typically a very small fraction of the flaw population). Because this is also a probabilistic calculation, it requires its own separate Monte Carlo sampling procedure within the larger Monte Carlo sampling procedure used to compute CPI.

Within this nested sampling process, a single random variable is sampled, which is used in the computation of K_{Ia} for each sample. A user-defined number of samples is taken, and $P(F|I)$ for that flaw is the total number of those samples that result in through-wall fracture propagation divided by the number of samples.

K_I Calculation for Propagating Cracks In the IGA model, it is assumed that all initiated cracks (either surface-breaking or embedded) immediately become infinite surface-breaking cracks. If any portion of the crack is located in the outer half of the vessel, immediate vessel failure is assumed, so CPF=CPI in those cases. For cracks that lie entirely in the inner half of the vessel, the infinite crack is assumed to be in the same orientation as the original flaw, and has a depth equal to the flaw depth in the case of surface-breaking cracks, or to the innermost depth of embedded cracks.

The through-wall dimension of the RPV is divided into a user-defined number of discrete increments of crack propagation. Starting at that initial depth, for each random realization, K_I is evaluated for an infinite surface-breaking crack at each of these depths until $K_I < K_{Ia}$, at which point the crack is assumed to arrest.

Fracture Arrest Reference Temperature The fracture toughness for fracture initiation is highly temperature dependent, and is based on the difference between the current temperature at the crack location, T and the nil-ductility reference temperature, RT_{NDT}:

$$T_{\mathrm{REL}} = T - RT_{\mathrm{NDT}} \tag{10}$$

The nil-ductility reference temperature is uncertain, and depends on material chemistry as well as exposure to irradiation, which increases that temperature, making the material more brittle. In the fracture initiation calculations, randomness due to multiple sources is accounted for in the sampled values for that parameter. By convention, sampled variables are indicated with a ˆ symbol over the variable name. Randomness is accounted for due to variability in the material properties (in the randomized initial reference temperature $\widehat{RT}_{\mathrm{NDT(0)}}$), epistemic uncertainty (in $\widehat{RT}_{\mathrm{epistemic}}$), and in embrittlement due to environmental exposure (in $\widehat{\Delta RT}_{\mathrm{NDT}}$):

$$RT_{\mathrm{NDT}} = \widehat{RT}_{\mathrm{NDT(0)}} - \widehat{RT}_{\mathrm{epistemic}} + \widehat{\Delta RT}_{\mathrm{NDT}} \tag{11}$$

The first two terms in this equation are computed in the initial generation of randomized variables for the CPI calculation, while the final term is dependent on fluence, and is computed using an embrittlement model later in the calculation.

The reference temperature specific for the arrest calculation is computed in a similar manner:

$$RT_{\mathrm{arrest}} = \widehat{RT}_{\mathrm{NDT(0)}} - \widehat{RT}_{\mathrm{epistemic\text{-}arrest}} + \widehat{\Delta RT}_{\mathrm{arrest}} + \widehat{\Delta RT}_{\mathrm{NDT}} \tag{12}$$

The only differences between the computation of RT_{arrest} and RT_{NDT} are that a different term is used to account for epistemic uncertainty, and the addition of the term $\widehat{\Delta RT}_{\mathrm{arrest}}$. Both of these terms re-use the random variable sampled for the computation of $\widehat{RT}_{\mathrm{epistemic}}$, and this computation is handled in essentially the same way that the computation for RT_{NDT} because the only term that is not computed in the initial sample generation is the last term, which accounts for local embrittlement. The full details of this sampling procedure are described in [1].

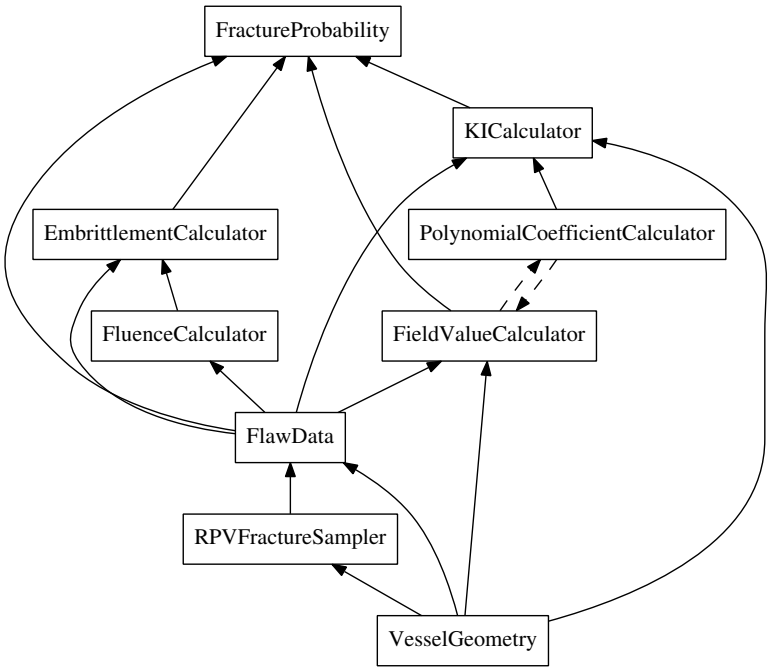

Figure 8: Modular structure of the components of the previously-implemented Grizzly PFM capability used for computing CPI, showing the dependencies between these components (adapted from [2]).

Computation of Randomized K_{Ia} K_{Ia} is dependent on the arrest relative arrest temperature:

$$T_{\text{REL-arrest}} = T - RT_{\text{arrest}} \tag{13}$$

which is in turn dependent on the local temperature and fluence. Thus, for each incremental depth at which a propagating crack is evaluated for a realization in the IGA model, K_{Ia} must be evaluated. A mean value for K_{Ia} is first evaluated as a function of $T_{\text{REL-arrest}}$. A single uniform variable generated for each sample in the IGA model is used to generate the sampled value of K_{Ia} used for determining whether arrest occurs. Again, the full details of this are described in [1].

2.3.2 Grizzly Implementation of IGA Model

Grizzly has a modular structure for its PFM calculations, which greatly facilitates management of the various components of that calculation, and provides the user significant flexibility to swap out new models for various components of that calculation to fit their individual needs. The major components of that structure for the CPI calculation (prior to the present work) are illustrated in Figure 8, which shows the dependencies of these modules on each other. The FractureProbability module is where CPI is ultimately computed, and as can be seen from the dependency diagram, it is the ultimate consumer of the computations performed by other modules, where quantities such as K_I and embrittlement are computed.

Figure 9 shows the modifications made to this modular structure to support the computation of CPF, with the added or modified modules highlighted. The changes to these modules are described below:

FailureProbability This newly added module computes $P(F|I)$ and CPF for flaws with nonzero CPI (which is computed in the FractureProbability module. The Monte Carlo sampling loop used for this probabilistic calculation, including the random variable sampling and computation of K_{Ia} for individual samples

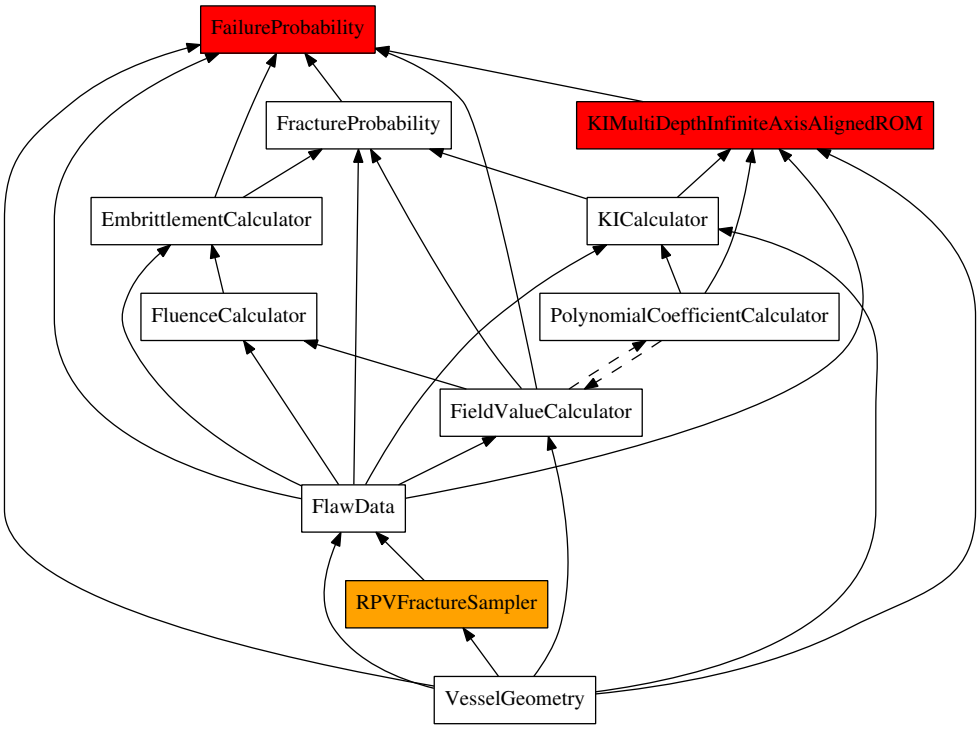

Figure 9: Modifications made to the modular structure that provides Grizzly's PFM capability made in the present work to support computation of CPF. Modules with major modifications are highlighted in orange, while newly added modules are highlighted in red.

resides in this class. This class also contains the code for incrementally advancing the crack through the RPV wall thickness and determining the fraction of realizations that result in through-wall fracture propagation.

KIMultiDepthInfiniteAxisAlignedROM This newly added module computes K_I for infinite inner surface-breaking cracks for arbitrary discrete depths through the wall of the RPV. This class derives from the same base class as the standard KICalculator classes used for computation of K_I for a single depth, but differs in a significant way from those classes because it can compute K_I at multiple depths, rather than only for the original flaw configuration.

RPVFractureSampler This class, which was modified for this new capability, is responsible for generating the randomized variables that describe the flaw population. The code that calculates all components of RT_{arrest} shown in Equation 12 with the exception of $\widehat{\Delta RT}_{\text{NDT}}$, which accounts for embrittlement, was added to RPVFractureSampler. These are not varied in the sampling used within the IGA model, so they can be computed up-front like the other randomized variables used in the PFM calculation.

2.3.3 Development Status

An ability to assess CPF for cleavage fracture has been fully developed in the modules described here. It should be noted that FAVOR also includes models for ductile fracture that are part of the IGA model, and those have not been implemented, although the structure outlined here will readily support that. Initial testing of these models on single flaw scenarios is underway. Future work is planned for thorough benchmarking of this capability full-scale RPV PFM analyses.

3 Cluster dynamics model for manganese rich precipitates in RPV steel

3.1 Introduction

Irradiation induced formation of Mn-Ni-Si precipitates (MNSPs) in low copper reactor pressure vessel (RPV) steels causes embrittlement and limits the operational life span. Aging research is being conducted in support of extending plant life to up to 80 years, with RPV embrittlement being a critical life extension issue.

MNSPs are part of a family of defects commonly referred to as *late blooming phases*. The emergence of these defects in the late stages of the RPV operational life time makes them particularly challenging to model. Large incubation times have to be modeled, necessitating coarse grained simulation methods that scale to long times. One such method is cluster dynamics, a mean field method that solves for the evolution of a cluster (precipitate) population in size space. Cluster dynamics allows for modeling nucleation, growth, and coarsening of precipitates. Fluxes between the different points in size space are computed. In the simplest case only monomers are assumed to be mobile. As a function of energy of formation and temperature adsorption and emission rates are computed.

Our focus is on low copper RPV steel, for which a cluster dynamics model has been developed by collaborators in the Morgan group at University of Wisconsin. The following two sections in this chapter will summarize the MNSCD model by Ke *et al.* [14] and the details of the model implementation in the MOOSE based Grizzly application. This has been implemented in Grizzly to facilitate its use in conjunction with other models for other aspects of the embrittlement problem.

3.2 Model

The MNSCD model by Ke *et al.* describes the evolution of the precipitate size distribution c_n in terms of incoming fluxes $J_{n-1\to n}$ and outgoing fluxes $J_{n\to n+1}$, where n is the cluster size in number of cluster atoms.

The model comprises two different cluster phases, the T3 $Mn_6Ni_{16}Si_7$ and the T6 $Mn(Ni,Si)_2$ phase. For each cluster phase subpopulations are tracked that emerged from homogeneous and heterogeneous nucleation. Clusters at all sizes are assumed to be at the exact stoichiometry corresponding to the phase they are in.

The MNSCD model implements heterogeneous nucleation as the instantaneous creation of clusters of size n_{het} at a rate proportional to a given radiation flux. Heterogeneous cluster creation depletes the monomer concentration to conserve mass. This heterogeneous nucleation is assumed to be driven by solute / point defect coupling in displacement cascades.

3.3 Implementation

The MNSCD model has been implemented in the MOOSE based Grizzly application. A standalone reference implementation [15] of the model was used for code to code verification.

- *Scalar kernels* in MOOSE implement weak form terms of ordinary differential equations.
  - `MNSCDComposition` implements the solute depletion due to the nucleation of new precipitates.
  - `MNSCDCluster` implements the $J_{n-1\to n} - J_{n\to n+1}$ contribution to the cluster size evolution ODE system.
  - `MNSCDMonomer` computes the monomer concentration as a function of the solute concentrations.
  - `MNSCDKernelBase` is a base class for the scalar kernels above.

- Postprocessor
  - `MNSCDMeanRadius` computes the size averages and number densities of cluster populations.
- User objects
  - `MNSCDParameters` holds the input parameters for the cluster dynamics model.
  - `MNSCDUpdate` holds derived and continuously updated quantities such as the fluxes between adjacent cluster sizes.
- Action
  - `MNSCDAction` is a MOOSE action object that assembles all objects required for an MNSCD simulation. The action creates all cluster and composition variables, sets the appropriate initial conditions, adds the scalar kernels to set up the ODE system, and sets up postprocessors for the output of averaged quantities.
- Initial conditions
  - `MNSCDSolutionProductIC` initializes the monomer concentration.
  - `MNSCDScalarConstantIC` initializes the composition variables with data from the parameter user object.
- *Time steppers* determine the simulation timestep dt to be taken by the MOOSE solver
  - `MNSCDTimeStepper` selects a quasi logarithmically growing timestep that reproduces the time stepping of the reference implementation [15] permitting direct comparisons.

The core design principle of the Grizzly MNSCD implementation is the encapsulation of the model input parameters and the state update into two separate user objects. Having the parameters in a user object will allow easy re-parameterization and tuning of the model while maintaining multiple concurrent versions for comparison. Having the bulk of the model computations centralized in a separate user object allows Grizzly to reduce redundant computations and avoid duplicate calculation of the fluxes to the clusters adjacent in size space.

The design and implementation of the model are complete and we are currently working on the code to code verification with the reference implementation. Small discrepancies remain and are subject to future investigation. The above figures show the time evolution of the cluster dimer concentrations (fig. 10) and the matrix solute concentrations (fig. 11). We are also looking into expanding and applying the MOOSE framework capabilities for automatic differentiation to the MOOSE ODE subsystem.

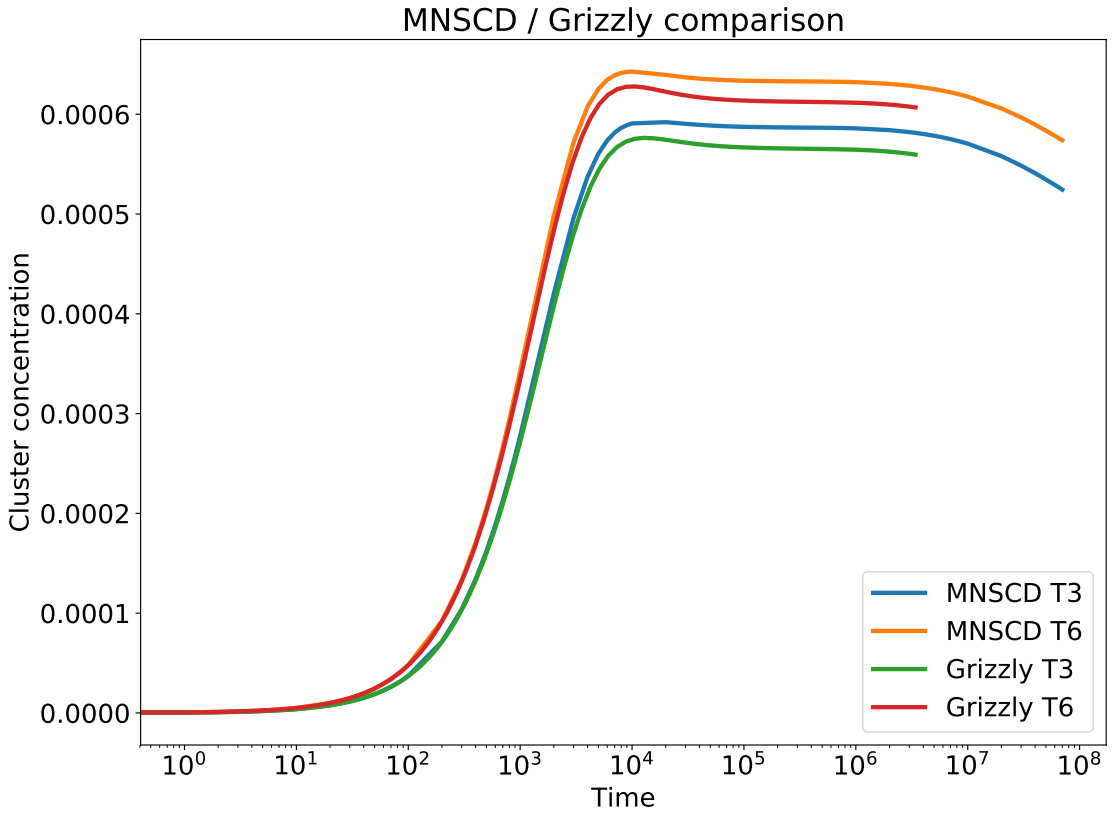

Figure 10: Comparing the dimer cluster concentrations for the T3 and T6 phases computed by the MNSCD reference implementation [15] and by Grizzly as a function of time.

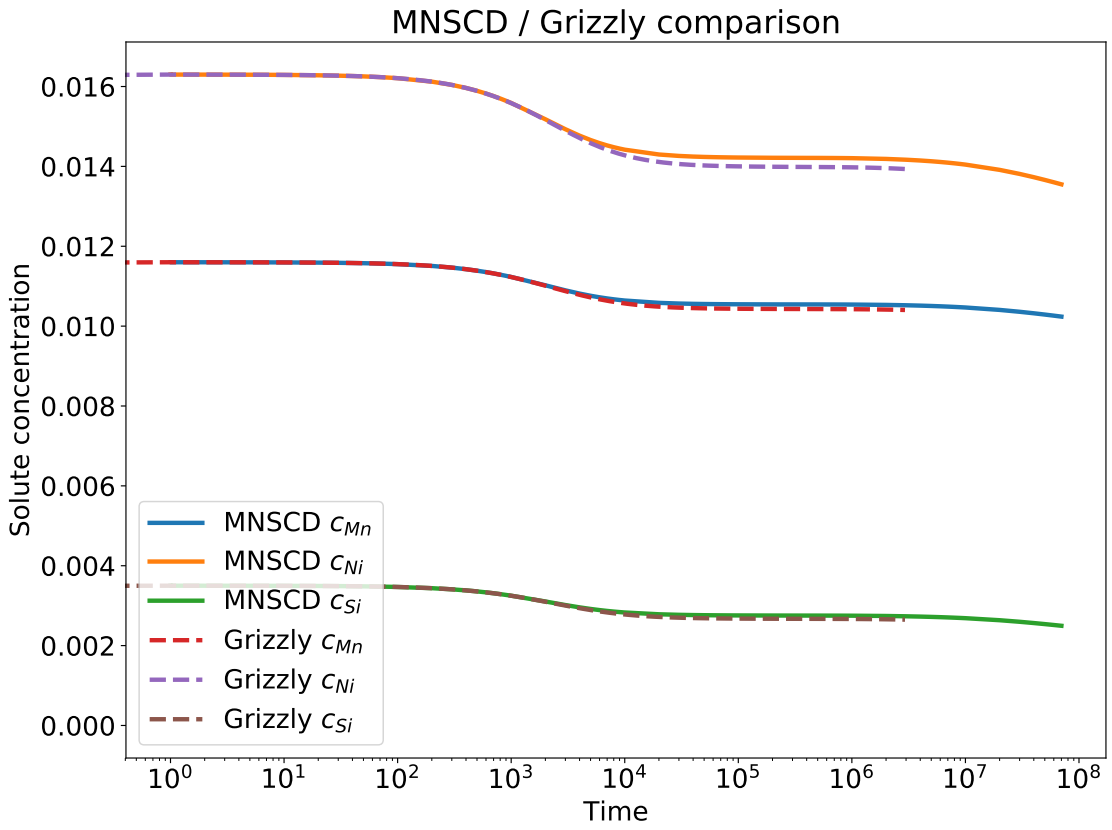

Figure 11: Comparing the MN, Ni, and Si solute concentrations in the iron matrix computed by the MNSCD reference implementation [15] and by Grizzly as a function of time.

4 Nonlinear Mechanical Models for Reinforced Concrete

Grizzly has a maturing capability for modeling the progression of aging mechanisms in reinforced concrete. Previous work has largely focused on the development of a framework for multiphysics modeling of the mechanisms leading to expansive reactions. Because expansive reactions such as ASR and RIVE lead to damage, it is also essential to have a robust capability for the nonlinear mechanical response of reinforced concrete. Some of the foundational capabilities for reinforced concrete mechanics were developed in fiscal year 2018, including creep and damage models, and a capability for modeling reinforcing bars that was limited to the elastic regime. This work has been continued in 2019, with further improvements to the concrete and reinforcing bar constitutive models. For concrete, the major development has been to permit the use of creep and damage models together, while for reinforcing bars, the major development was to add the ability to model material nonlinearity. The details of this work are described here.

4.1 Concrete Constitutive Model Development

4.1.1 Damage Model

Failure in concrete occurs due to accumulation of microcracks and can be captured using an isotropic damage model. Grizzly uses the Mazars damage model, which represents the degradation of the elasticity tensor of the concrete using an isotropic damage index. The model determines the evolution of damage depending on the total strain experienced by the material under tensile or compressive loading. Separate damage variables for tension (d_t) and compression (d_c) are computed as

$$d_t = 1 - \frac{\kappa_0(1 - A_t)}{\kappa} - \frac{A_t}{\exp[B_t(\kappa - \kappa_0)]}\,, \tag{14}$$

and

$$d_c = 1 - \frac{\kappa_0(1 - A_c)}{\kappa} - \frac{A_c}{\exp[B_c(\kappa - \kappa_0)]} \tag{15}$$

where A_t, A_c, B_t, and B_c are material parameters that control the shape of the nonlinear response and are determined using compression and tension tests. The parameter κ defines the threshold of damage growth with κ_0 being its initial value determined from f_t/E_0, where f_t is the tensile strength and E_0 is the initial Young's modulus of the material. During subsequent steps, it takes on the maximum value of the equivalent strain during the entire load history

$$\kappa = \max(\tilde{\varepsilon}, \kappa_0)\,. \tag{16}$$

Here, the equivalent strain is calculated from the positive eigenvalues of the total strain tensor as

$$\tilde{\varepsilon} = \sqrt{\sum_{i=1}^{3} (\langle \varepsilon_i \rangle_+)^2}, \tag{17}$$

where ε_i are the components of the principal strain and $\langle \varepsilon_i \rangle_+$ provided only the positive value of the strains.

The damage criterion is determined based on the following relation:

$$f(\tilde{\varepsilon}, \kappa) = \tilde{\varepsilon} - \kappa\,. \tag{18}$$

The effective damage behavior is expressed in terms of the scalar damage index represented by a combination of damage characteristics of the concrete in tension and in compression

$$d = \alpha_t d_t + \alpha_c d_c\,, \tag{19}$$

where α_t and α_c are dimensionless coefficients and represent the contribution of each loading mode such that $\alpha_t = 1$ and $\alpha_c = 0$ under uniaxial tension, and $\alpha_t = 0$ and $\alpha_c = 1$ under uniaxial compression. These coefficients are defined as functions of the principal components of the strain tensors and are computed as

$$\alpha_t = \sum_{i=1}^{3} \left(\frac{\langle \varepsilon_i^t \rangle \langle \varepsilon_i \rangle}{\tilde{\varepsilon}^2} \right), \tag{20}$$

and

$$\alpha_c = \sum_{i=1}^{3} \left(\frac{\langle \varepsilon_i^c \rangle \langle \varepsilon_i \rangle}{\tilde{\varepsilon}^2} \right). \tag{21}$$

4.1.2 Creep Model

Creep deformation in concrete is observed due to constant loading over time. Creep is facilitated by the external conditions such as temperature, moisture etc. that lead to the shrinkage of the concrete over time. The creep behavior of the concrete material is modeled based on the generalized Kelvin-Voigt model. Here, the system is presented by a combination of springs and dashpots connected in a series. The visoelastic behavior of the dashpots deteriorate the stiffness of the concrete. The overall stress-strain behavior is expressed as

$$\sigma_{ij} = \left(C_{ijkl} \varepsilon_{kl}^{mech} - \sum_{n=1}^{N} C_{ijkl}^{n} \alpha_{kl}^{n} \right). \tag{22}$$

The α^n are the internal strains associated with each Kelvin-Voigt unit and C^n is the stiffness of the corresponding spring in the chain. The unit obey the following time-dependent relation

$$\forall n \in [1, N] \, : \, \sigma_{ij}^{n} = C_{ijkl}^{n} \left(\alpha^n + \eta^n \dot{\alpha}^n \right), \tag{23}$$

where η^n is the viscosity of the associated dashpot. The constitutive equations are solved using a semi-implicit single-step first-order finite difference scheme. The internal strains at time step $t + \Delta t$ are computed from their values at the previous time step t as

$$\alpha^n(t + \Delta t) = \alpha^n(t) + \Delta t \left[\theta^n \dot{\alpha}^n(t + \Delta t) + (1 - \theta^n) \, \dot{\alpha}^n(t) \right]. \tag{24}$$

Here, θ is a scalar between 0 (fully explicit) and 1 (fully implicit) that controls the time-stepping scheme.

Further, the logarithmic viscoelastic behavior for concrete has been implemented assuming a Burgers type of material with an elastic spring, a Kelvin-Voigt module, and a dashpot placed in series. The total strain is decomposed into three components: an elastic strain ε_e, a recoverable viscoelastic strain ε_r and an irrecoverable creep strain ε_c such that

$$\varepsilon = \varepsilon_e + \varepsilon_r + \varepsilon_c \, . \tag{25}$$

The elastic strain is directly related to the stress σ with the usual Hooke's law, where C_e is the fourth-order elasticity tensor of the material.

$$\sigma = C_e \, : \, \varepsilon_e \tag{26}$$

The recoverable creep strain corresponds to the short-term visco-elastic strain of the material, which can be partially recovered upon unloading. It is calculated using a single Kelvin-Voigt module,

$$\sigma = C_r \, : \, \left(\varepsilon_r + \eta_r \dot{\varepsilon}_r \right) \tag{27}$$

where C_r is the fourth-order elasticity tensor of the spring and η_r the viscosity of the dashpot. Irrecoverable creep strain corresponds to the long-term visco-elastic strain of the material. It is linear with the logarithm of time, and cannot be recovered upon unloading. It is calculated as

$$\sigma = \left(1 + \frac{t}{\tau_c}\right) \eta_c C_e : \dot{\varepsilon}_c \,, \tag{28}$$

where η_c is the viscosity of the time dependent dashpot and τ_c is the characteristic time of the logarithmic creep that controls when the logarithmic behavior starts. Furthermore, the model also include the effect on temperature, a constant low relative humidity and drying on creep.

4.1.3 Combining Creep and Damage Model

A two way coupling between creep and damage is established in the current model. The damage index is calculated based on the total strain which constitute of the elastic as well as the creep strain. However, only part of the creep strain could contribute towards the damage. Thus, the total strain used for the damage calculation is expressed as

$$\varepsilon = \varepsilon_e + \alpha \varepsilon_{cr} \,. \tag{29}$$

Here, α is a factor between 0 (no coupling) and 1 (total coupling) to determine the contribution of the creep strain (ε_{cr}).

The damage parameter degrades the stiffness of the material and overall reduces the stress experienced by the material. The effective stress is calculate as

$$\sigma = (1 - d)\sigma_0 \,, \tag{30}$$

where σ_0 is the undamaged stress. The inelastic model is executed on the undamaged stress and the final stress is reduced based on the damage variable. To avoid numerical challenges, the stress reduction is done based on the damage variable from previous timestep.

4.2 Nonlinear Behavior of Reinforcement Bars

The reinforcement bars in the concrete are modeled using 1D truss elements. The model utilizes a discrete finite element implementation strategy to simplify the computational effort. The axial elongation of the element is obtained from

$$\varepsilon = \frac{\Delta l}{l_0} = \frac{(l - l_0)}{l_0} \,, \tag{31}$$

where δl is the total stretch computed from the updated length of the element and the old length. In case of linear elastic material the axial stress is computed as

$$\sigma_a = E \frac{\Delta l}{l_0} \,. \tag{32}$$

The nonlinear behavior of the reinforcement bar is implemented using a simplistic J2 plasticity model with linear hardening. The strain increment is obtained from the total stretch update

$$\Delta\varepsilon = \varepsilon - \varepsilon_{old} \,. \tag{33}$$

The trial stress is estimated as

$$\sigma^{tr} = \sigma_{old} + E\Delta\varepsilon \,. \tag{34}$$

The effective trial stress is

$$\tilde{\sigma}^{tr} = \sqrt{\frac{2}{3}\sigma^{tr}\sigma^{tr}}\,. \tag{35}$$

The yield condition is determined as

$$f = \tilde{\sigma}^{tr} - 3G\Delta p - r - \sigma_y = 0\,, \tag{36}$$

where G is the shear modulus, r is the linear hardening function defined as $r = hp$ with h being the hardening constant, σ_y is the yield stress. For the effective trial stress being outside of the yield profile the stresses are brought down using the iterative Newton method. The hardening variable at the beginning of the iterative process is obtained as

$$r^k = r_{old} + h\Delta p^k\,. \tag{37}$$

The effective plastic strain increment is computed as

$$d\Delta p = \frac{f}{\frac{df}{d\Delta p}} = \frac{(\tilde{\sigma}^{tr} - 3G\Delta p^k - r^k - \sigma_y)}{3G + h} = 0\,. \tag{38}$$

The effective plastic strain for the next iteration is updated

$$\Delta p^{(k+1)} = \Delta p^k + d\Delta p\,. \tag{39}$$

The iterative process continues until the updated stress lies on the yield curve. The inelastic strain is calculated as

$$\Delta\varepsilon^p = \sqrt{\frac{3}{2}\Delta p\Delta p}\,. \tag{40}$$

The elastic strain is updated as

$$\Delta\varepsilon^e = \Delta\varepsilon - \Delta\varepsilon^p\,. \tag{41}$$

The updated axial stress is calculated

$$\sigma_a = \sigma_{old} + E\Delta\varepsilon^e\,. \tag{42}$$

4.3 Model Testing

Several test cases are created to verify that the developed models were implemented correctly. The combined effect of creep and damage is evaluated based on the behavior of a single element model as well as a large morel more representative of a reinforced concrete member. Here, first we present the behavior of a concrete plate with no reinforcement under uniaxial loading. A schematic of the problem is shown in Figure 12. The

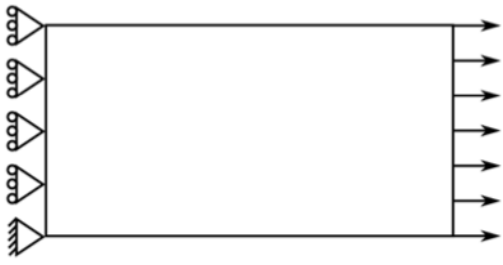

Figure 12: Concrete plate under uniaxial loading

plate is evaluated under both tensile and compressive loading. Comparing the plate's response during linear

elastic and creep deformation, it can be seen that creep only affects the evolution of damage in tension and not in compression. However, in both cases the overall stress-strain behavior is significantly affected by the creep deformation. Including the effects of creep significantly reduces the stress withstood by the plate in both tension and compression.

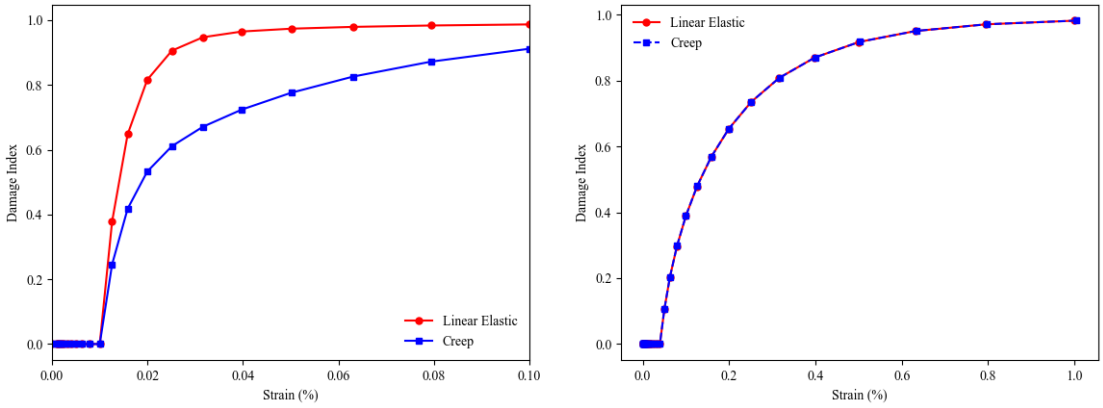

(a) (b)

Figure 13: Damage evolution of the simple concrete plate under uniform (a) tension, and (b) compression, with and without the creep model.

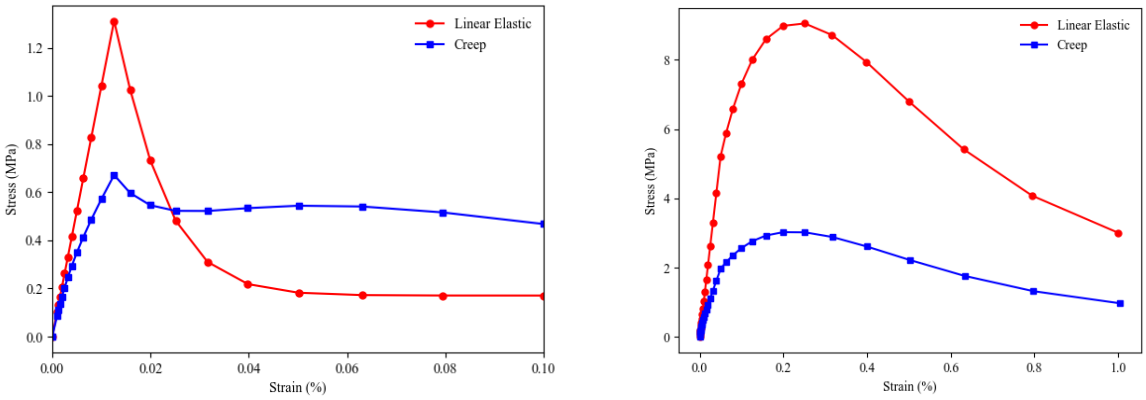

Figure 14: Stress/strain behavior of the simple concrete plate under uniform (a) tension; (b) compression, with and without the creep model.

Figure 15 demonstrates the inelastic behavior of a single 1D truss element loaded in tension. A linear hardening behavior is observed when the yield stress is exceeded.

A simple model of a reinforced concrete beam has been tested to demonstrate the effect of reinforcement bars on the tensile behavior of a reinforced concrete member. Two variants of this model, with and without rebar, were subjected to tensile loading. 16 shows the deformation of both variants of this model. The displacements are amplified with a factor of 20 for visualization purposes. 17 depicts the load displacement behavior of the right end of the beam in both the cases. These preliminary results show that Grizzly can run this type of model, and that as would be expected, reinforcing bars strengthen the concrete structure

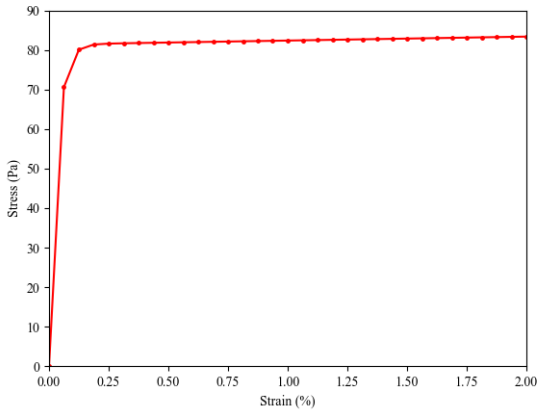

Figure 15: Stress/strain behavior of a truss element capturing the nonlinear inelastic behavior.

and delay its failure. Future work is planned to develop a set of validation problems to rigorously test these models and assess how well they compare with experimental results.

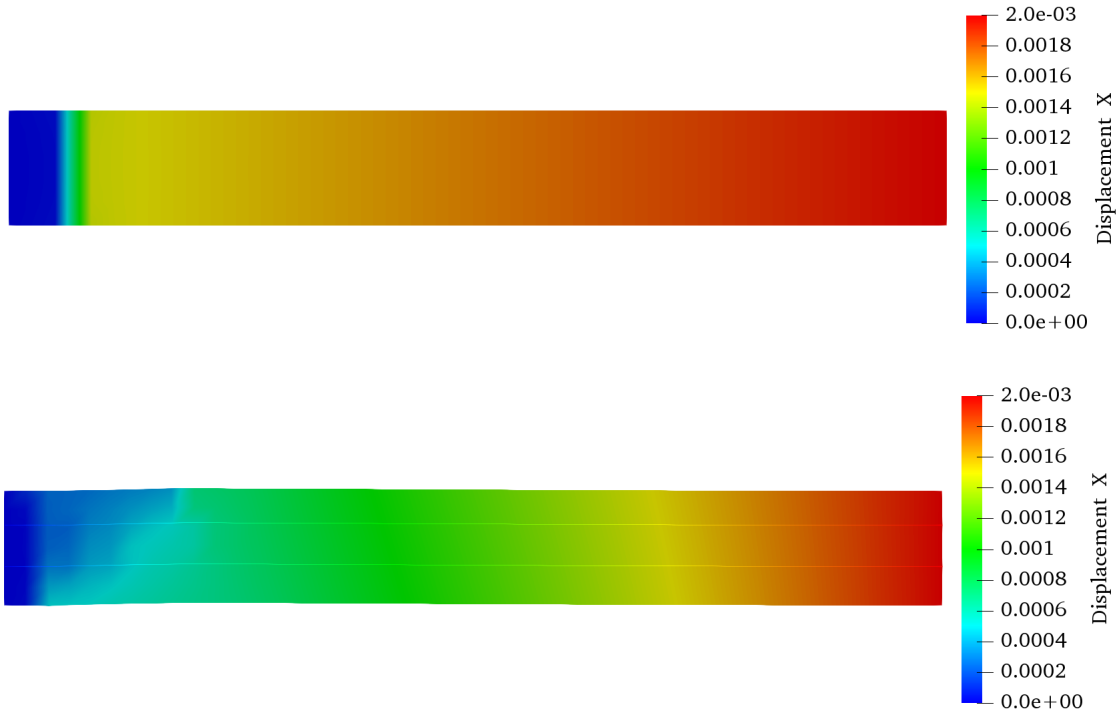

Figure 16: Deformation of simple beam model under tensile loading showing (top) the behavior of a version of the model with no reinforcement and (bottom) the behavior of the model with reinforcement. The presence of the reinforcement clearly has a strengthening effect, distributing the damage that is localized in the unreinforced case over a larger area.

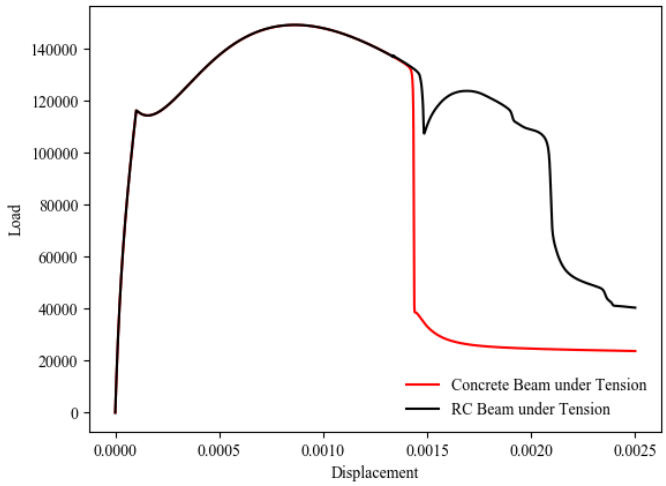

Figure 17: Load displacement behavior of the concrete beam under uniaxial tension, showing the strengthening effect.

5 Summary

This report documents the addition of features for Grizzly in the following major areas:

For engineering-scale PFM analysis, models were added to capture the effects of the warm prestressing phenomenon, residual stresses, and crack arrest. All of these models followed the approaches of the FAVOR code. In the case of warm prestressing, including this effect tends to make the models less conservative, because warm prestressing has a strengthening effect, so neglecting it results in higher predicted CPI. Because residual stresses in weld regions increase the stress intensity factors at flaws, including their effect is important to avoid under-representing CPI. The crack arrest model permits calculation of CPF, which is important for fully understanding the consequences of a given transient loading, in addition to CPI. These capabilities have been tested to varying degrees on single flaw analyses, but still need to be fully tested in large-scale PFM calculations with large flaw populations. An extensive benchmarking study is planned to ensure that Grizzly calculations are correct with a variety of combinations of models on representative full RPV geometries.

An existing cluster dynamics model for MNSPs has been implemented in Grizzly. Grizzly already had a cluster dynamics model for copper rich precipitates, as well as capabilities for modeling precipitate nucleation, growth, and coarsening using atomistic and phase field models. Now that these models are implemented, they will be examined in depth to determine which parameters are the most important and which have the greatest uncertainty, so that future work can be planned to address these needs.

Finally, developments were made to Grizzly's engineering-scale capabilities for reinforced concrete to improve the constitutive models for the nonlinear response of both concrete and reinforcement. Code changes were made to permit simultaneous use of the damage and creep models, which is important for correctly modeling the effects of degradation mechanisms that can occur over long time frames. Nonlinear behavior of reinforcing steel is also now represented. Grizzly now has models for most of the important mechanisms affecting nonlinear mechanical response. The last major missing capability is a bond slip model for use together with the 1D rebar models. This will fit naturally within Grizzly's framework for modeling rebar, which uses constraints to connect rebar to the concrete matrix. This is the next planned development in this area. Testing to validate Grizzly models against results of experiments on structural components is also planned.

6 References

[1] P. Williams, T. Dickson, B. R. Bass, and H. B. Klasky. *Fracture Analysis of Vessels – Oak Ridge, FAVOR, v16.1, Computer Code: Theory and Implementation of Algorithms, Methods, and Correlations*. Tech. rep. ORNL/LTR-2016/309. Oak Ridge, TN: Oak Ridge National Laboratory, Sept. 2016.

[2] B. Spencer, W. Hoffman, and M. Backman. "Modular system for probabilistic fracture mechanics analysis of embrittled reactor pressure vessels in the Grizzly code". In: *Nuclear Engineering and Design* 341 (Jan. 2019), pp. 25–37.

[3] D. Gaston, C. Newman, G. Hansen, and D. Lebrun-Grandié. "MOOSE: A parallel computational framework for coupled systems of nonlinear equations". In: *Nuclear Engineering and Design* 239.10 (Oct. 2009), pp. 1768–1778.

[4] G. Qian, M. Niffenegger, M. Sharabi, and N. Lafferty. "Effect of non-uniform reactor cooling on fracture and constraint of a reactor pressure vessel". In: *Fatigue & Fracture of Engineering Materials & Structures* (Mar. 2018).

[5] V. Lacroix and P. Dulieu. "Structural Integrity Assessment of Doel 3 and Tihange 2 RPVs Affected by Hydrogen Flakes: Methodology and Results". In: ASME, July 2016, V01AT01A058.

[6] B. W. Spencer, W. M. Hoffman, B. S. Collins, and S. C. Henderson. *Use of Neutron Flux Calculated by Shift in a Grizzly Reactor Pressure Vessel Fracture Simulation*. Tech. rep. INL/EXT-19-55617, CASL-U-2019-1898-000. Idaho National Laboratory, Sept. 2019.

[7] *The Demonstration of Warm Prestress Effect in RPV Assessment: Some Experimental Results and Their Interpretation by Fracture Mechanics*. ASTM/ESIS, Nov. 2007.

[8] J. Keeney, B. Bass, W. McAfee, and S. Iskander. *Preliminary Assessment of the Fracture Behavior of Weld Material in Full- Thickness Clad Beams*. Tech. rep. NUREG/CR-6228; ORNL/TM-12735. Oak Ridge, TN: Oak Ridge National Laboratory, Oct. 1994.

[9] W. Pennell. *Heavy-Section Steel Technology Program: Semiannual Progress Report for October 1996-March 1997*. Tech. rep. NUREG/CR-4219 14(1); (ORNL/TM-9593/V14&N1). Oak Ridge, TN: Oak Ridge National Laboratory, 1997, pp. 36–39.

[10] H. F. Bückner. "A novel principle for the computation of stress intensity factors". In: *Z. angew Math. Mech.* 50 (1970), pp. 529–546.

[11] S. X. Xu, R. C. Cipolla, D. R. Lee, and D. A. Scarth. "Improvements in Article A-3000 of Appendix A for Calculation of Stress Intensity Factor in Section XI of the 2015 Edition of ASME Boiler and Pressure Vessel Code". In: *Journal of Pressure Vessel Technology* 139.1 (Aug. 2016), p. 010801.

[12] S. X. Xu, D. R. Lee, D. A. Scarth, and R. C. Cipolla. "Update on Stress Intensity Factor Influence Coefficients for Axial ID Surface Flaws in Cylinders for Appendix A of ASME Section XI". In: *Proceedings of the ASME 2015 Pressure Vessels and Piping Conference*. PVP2015-46009. ASME, July 2015.

[13] *Section XI, Rules for Inservice Inspection of Nuclear Power Plant Components, Nonmanditory Appendix A, Article A-3000 Method of K_I Determination*. American Society of Mechanical Engineers Boiler and Pressure Vessel Code. American Society of Mechanical Engineers, 2017.

[14] H. Ke, P. Wells, P. D. Edmondson, N. Almirall, L. Barnard, G. R. Odette, and D. Morgan. "Thermodynamic and kinetic modeling of Mn-Ni-Si precipitates in low-Cu reactor pressure vessel steels". In: *Acta Materialia* 138 (2017), pp. 10–26.

[15] H. Ke. *Cluster Dynamics code for evolution of Mn-Ni-Si in low-Cu RPV steels*. `https://github.com/uw-cmg/MNS_CD`. 2018.